IEEE Access
Multidisciplinary ⋮ Rapid Review ⋮ Open Access Journal

Date of publication xxxx 00, 0000, date of current version xxxx 00, 0000.

Digital Object Identifier 10.1109/ACCESS.2020.Doi Number

Equivalent-Circuit-Based Design of Symmetric Sensing Coil for Self-Inductance-Based Metal Object Detection

Van X. Thai[1], Jun H. Park[2], Seog Y. Jeong[2], Member, IEEE, Chun T. Rim[3], Fellow, IEEE, and Yun-Su Kim[3], Member, IEEE

[1]Oceansbio, Seoul, South Korea
[2]Samsung Electronics, Seoul, South Korea
[3]School of Integrated Technology, Gwangju Institute of Science and Technology (GIST), Gwangju 61005, South Korea

Corresponding author: Yun-Su Kim (e-mail: yunsukim@gist.ac.kr).

This work was supported by the "Practical Research and Development support program supervised by the GTI (GIST Technology Institute)" grant funded by GIST in 2020.

ABSTRACT A symmetric sensing coil design is proposed and adapted for the self-inductance-based metal object detection (MOD) of wireless electric vehicle (WEV) charging. Compared to conventional non-symmetric sensing coils, the proposed sensing coil provides symmetric detection sensitivity and ease of manufacturing, pertaining blind-zone-free characteristics. Moreover, it is found that the design of the proposed symmetric sensing coil is very different from that of the symmetric sensing coil for conventional induced voltage sensing (IVS) based MOD method due to different principles of MOD methods. Therefore, an analysis based on a newly proposed equivalent circuit, is used to design a high sensitivity symmetric sensing coils, considering many aspects such as metal object covering, metal object size, and mutual inductance between sensing coils. Based on the analysis, an optimized sensing coil design created through a finite element method simulation is proposed to achieve highest sensitivity with the lowest number of sensing coils. It can be readily applied to a cost-effective MOD system that can be used for high-power WEV charging. Experiments on a metal object 20 mm × 20 mm in size with a $20A_{rms}$ Tx current verified high detection sensitivity of 38% without any blind zones.

INDEX TERMS Foreign object detection, metal object detection, inductive power transfer, wireless electric vehicle

I. INTRODUCTION

Inductive power transfer (IPT) for wireless electric vehicle (WEV) charging involves managing significant technical issues, such as the power transfer capability, efficiency, and tolerances [1]-[11]. Specifically, safety and reliability issues such as electromagnetic field (EMF) cancellation [12]-[15] and foreign object detection (FOD) [16]-[33] are crucial for WEV commercialization. While EMF cancellation provides safety for humans by reducing or shielding the EMF generated by an IPT system, FOD is mainly related to the safety and reliability of IPT systems themselves by detecting objects which may harm the system.

For IPT systems, the most dangerous types of foreign object are typically made of metal. If a metal object such as a gum wrapper or a coin were to end up on the transmitting (Tx) pad of an IPT system when the system is charging, its temperature can rise rapidly due to the induced eddy current to the point that the metal object eventually ignites, damaging the system or even injuring people. Because metal objects pose such a serious threat to these systems, various methods have been suggested in order to detect the existence of metal objects on a Tx pad [16]-[33]. These methods are collectively known as metal object detection (MOD), which is one of the main branches of FOD methods.

Conventional MOD methods for WEV charging can be categorized based on physical operating principle. The first group of methods evaluates parameter changes of an IPT system, such as the Q-factor, resonant frequency, and coil voltage, to determine the existence of metal objects [16]-[20].

This article has been accepted for publication in a future issue of this journal, but has not been fully edited. Content may change prior to final publication. Citation information: DOI 10.1109/ACCESS.2020.2995210, IEEE Access

Although these methods are easy to implement, detecting small metal objects is difficult because the Tx coil is much larger than typical metal objects and changes in system parameters are minute for small metal objects. The second type of method, applied to the Qi standard for FOD, compares the expected receive power with the measured receive power to detect metal objects [21]. However, these methods can only be used when the air gap is quite small and the magnetic coupling is strong, as dictated by the Qi standard; hence, they are not suitable for WEV charging, where the air gap is not small and can vary. The third method is to use additional devices such as radar, thermal cameras, and video cameras; but these systems are expensive, easily contaminated, and difficult to integrate into IPT systems [22]-[27].

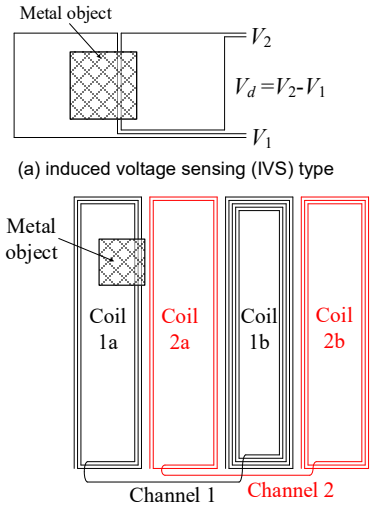

FIGURE 1. Conventional MOD methods of magnetic field change sensing (MFCS).

While the three methods mentioned above are either insensitive to small metal objects or too expensive, another group of cost-effective methods using magnetic field change sensing (MFCS), as shown in Figure 1, offers many advantages favorable to WEV charging [28]-[33]. In general, MFCS methods can be divided into two types.

The first is the induced voltage sensing (IVS) type, which utilizes the induced voltage difference between two loop coils due to metal objects for the magnetic field generated by the Tx current, as shown in Figure 1(a) [28]-[32]. The induced voltage difference V_d is roughly proportional to the size of the metal object [29]. The IVS type provides an inexpensive and simple solution for WEV charging given its ability to detect small metal objects. However, this type is also associated with the blind zone problem. When metal objects are positioned between two coils, they cannot be detected. Overcoming the blind zone problem is expensive and requires complicated tasks [29]-[31]. In order to solve the blind-zone problem, a cost-effective and simple solution, which utilizes a symmetric sensing coil to detect metal objects, is proposed in [32]. By arranging the sensing coils into several channels, each of which includes a pair of symmetric sensing coils, the blind-zone between two adjacent sensing coils can be eliminated effectively. However, although the blind-zone problem can be solved by modifying the sensing coils, the IVS type still has a big disadvantage since it cannot work when the IPT system is turned off, as the magnetic field does not exist.

The second type consists of self-inductance-based resonant circuit (SIRC) methods. These approaches utilize parallel resonant circuits that amplify the self-inductance change, as shown in Figure 1(b) [33]. They can resolve the two aforementioned problems of the IVS type. SIRC methods have no blind zone due to the two overlapped sensing coils and are self-activated by the current source instead of the Tx current, thus enabling independent operation from the powering of the IPT system. Moreover, because the distance between Rx pad and sensing coils and much farther than the distance between the metal objects and the sensing coils, the effect of Rx pad misalignment on the self-inductance change of the sensing coils is negligible.

Despite the superiority of the SIRC type over the IVS type, the sensing coil design of an earlier SIRC type [33] has a few drawbacks, which prevent its practical application. In the SIRC design, in order to cancel out the induced voltage caused by an unequal Tx magnetic field, the numbers of turns in two sensing coils in one channel differ from one another, as shown in Figure 1(b). As a result, the sensitivity of two sensing coils of one channel is not the same, which means that the sensitivity of one sensing coil can be low. This allows the existence of blind-zone where the sensitivity is too low to detect the metal object. Moreover, manufacturing and designing the sensing coils becomes difficult and complicated when the configuration of the Tx coil is irregular and not uniform, thus necessitating a redesign of the number of turns for every channel. Furthermore, in many cases, because the magnetic flux through one sensing coil can be very large compared to the other sensing coil, changing the number of turns of sensing coils is ineffective in reducing induced voltage.

In this paper, in order to resolve all of the aforementioned problems associated with SIRC methods, the idea of symmetric sensing coil, which was firstly proposed in [32], is adapted to the SIRC type. With the symmetric sensing coil design, every sensing coil has an identical number of turns; hence, induced voltage becomes zero automatically, manufacture and design the sensing coil become much easier, the adjustment of the number of turns is unnecessary, and most importantly, the detection sensitivity over the entire Tx pad can become symmetric, which reduces the risk of blind-zone existence. Although it stems from the symmetric sensing coil idea in [32], the design of the symmetric sensing coil proposed in this paper is very different from the sensing

This article has been accepted for publication in a future issue of this journal, but has not been fully edited. Content may change prior to final publication. Citation information: DOI 10.1109/ACCESS.2020.2995210, IEEE Access

coil design for IVS type due to the fact that the principle of IVS and SIRC methods are different. Therefore, an equivalent circuit of the proposed sensing coil considering the metal object covering is newly proposed and analyzed in order to clarify the difference of the two designs. Moreover, by analyzing the effect of the mutual inductance between sensing coils and the influence of metal object size on the sensitivity, an optimization of the proposed symmetric sensing coil is also proposed. The analysis and optimization are verified by the FEM simulations and power experiments with 3.3 kW IPT system for WEV charging at the Tx current of 20 A_{rms}.

II. CONCEPT OF THE PROPOSED SYMMETRIC SENSING COIL

The concept of the proposed sensing coil design is shown in Figure 2.

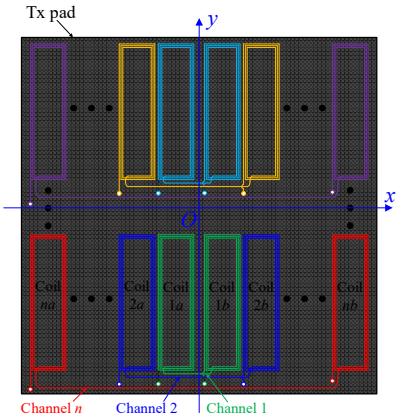

FIGURE 2. Conceptual design of the proposed symmetric sensing coil. Channels are differentiated by the different colors. Each channel includes two sensing coils, which have same number of turns and which are shown in the same color.

The proposed sensing coils are composed of many channels. Each channel includes two sensing coils connected in series with opposite polarities to cancel out the induced voltage generated by the Tx coil current. This is the main advantage of the multiple series coil design compared to single coil design as the induced voltage can saturate the output voltage of the op-amp of the sensing circuit. However, instead of installing two sensing coils of one channel very close to each other, as in Figure 1(b), the two sensing coils in the proposed design are set up symmetrically about the y-axis of the Tx pad, as shown in Figure 2. This is done because the z direction component of the magnetic flux generated by the Tx coil current is symmetrical about y-axis of the Tx pad, as verified by the finite element method (FEM) simulation shown in Figure 3(a). As indicated in the figure, the magnetic flux density in the z direction is distributed symmetrically about the y-axis. Therefore, the voltages induced on the two sensing coils of each channel will be identical and can cancel each other out if the two sensing coils are connected in an opposite polarity configuration. For illustration, an FEM simulation model with 24 channels consisting of 48 sensing coils was built by ANSYS Maxwell 15.2, as shown in Figure 3(b). The induced voltages of the two sensing coils in the single channel are identical, as shown in Figure 3(c).

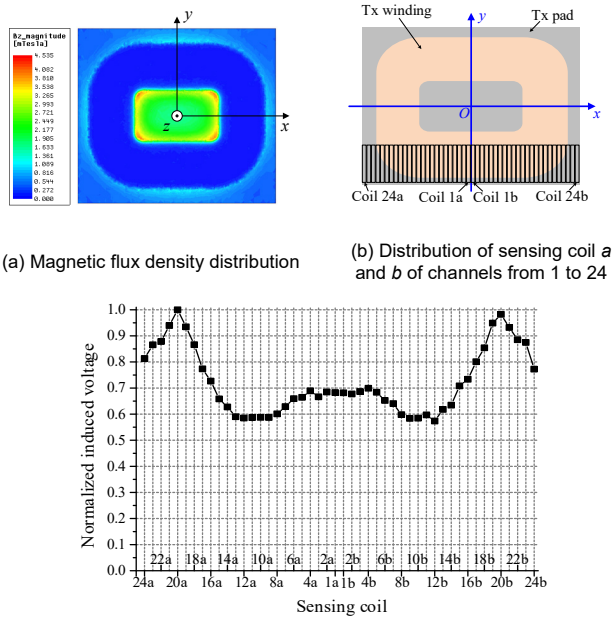

(a) Magnetic flux density distribution

(b) Distribution of sensing coil *a* and *b* of channels from 1 to 24

(c) Normalized induced voltages of the sensing coils

FIGURE 3. FEM simulation showing the symmetrical distribution about the y-axis of the z-direction magnetic flux density generated by the Tx coil current.

The obvious advantages of this design are the simplicity of the sensing coil design and the easy manufacturing process. Instead of adjusting the number of turns of every channel to nullify the induced voltage, the induced voltage is automatically nullified in the new design as long as the numbers of turns of sensing coils are identical.

III. MODELING THE PROPOSED SYMMETRIC SENSING COIL

In order to understand how the impedance of sensing coil is changed by a metal object, and the difference between a symmetric sensing coil in SIRC type and IVS type, a model of sensing coils considering the effect of metal objects should be built. An equivalent circuit has been proposed in [33], but it oversimplifies the model when it considers a channel as a single inductor. Therefore, it fails to clarify the interaction between two sensing coils and the interaction of metal object with each sensing coil. In this section, an equivalent circuit of two sensing coils of one channel is thoroughly built considering all possible cases of position of metal object on the sensing coils: when metal object is on only one sensing coil of a channel, and when a metal object is on both sensing coils of one channel.

A. EQUIVALENT CIRCUIT WHEN METAL OBJECT IS ON ONE SENSING COIL OF A CHANNEL

In most cases, a metal object is small compared to a sensing coil, and two sensing coils of one channel is usually far from each other. Therefore, the case that a metal object is on only one sensing coil of a channel becomes the most popular case as a metal object is on the Tx pad. Considering a channel *k* with two sensing coils *ka* and *kb* as shown in Figure 4, a metal object is either on coil *ka* or on coil *kb* as shown in Figures 4(a) and 4(b), respectively.

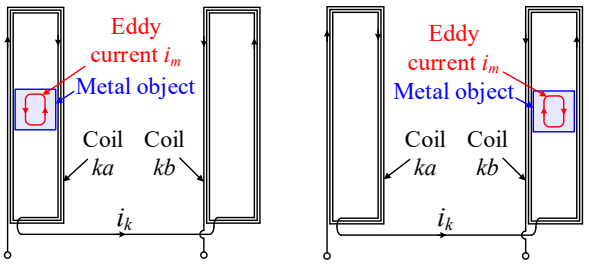

(a) when the metal object is on sensing coil *ka* (b) when the metal object is on sensing coil *kb*

FIGURE 4. Two cases of when a metal object is on only one sensing coil of channel *k*.

The equivalent circuit of the channel considering the metal object can be built as shown in Figure 5.

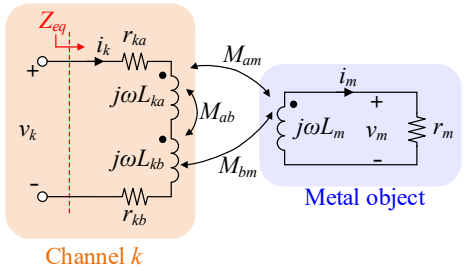

FIGURE 5. Equivalent circuit model of one channel *k* in case of metal object is on only one sensing coil.

In Figure 5, two sensing coils, coil *a* and coil *b*, of channel *k* are represented by two series inductors, L_{ka} and L_{kb}, and two internal resistors, r_{ka} and r_{kb}; the metal object is modelled as an inductor, L_m, in series with an internal resistor, r_m. The mutual inductances between the metal object and the two sensing coils are M_{am} and M_{bm}, respectively. When the metal object is on coil *a*, M_{bm} becomes zero; when the metal object is on coil *b*, M_{am} becomes zero. The mutual inductance between coil *a* and coil *b* is M_{ab}. When there is no metal object, both M_{am} and M_{bm} are null; hence, the equivalent impedance of the channel is given as

$$Z_{eq,wo} = r_k + j\omega(L_{ka} + L_{kb} + 2M_{ab}) = r_k + j\omega L_k \quad (1)$$

where the subscript "*wo*" denotes "without a metal object" and r_k and L_k are the total resistance and total inductance of the two sensing coils of the channel. These are defined as follows:

$$r_k = r_{ka} + r_{kb} \quad (2a)$$
$$L_k = L_{ka} + L_{kb} + 2M_{ab} \quad (2b)$$

When a metal object is present, amplitude voltage V_k of channel *k* and amplitude voltage V_m on the metal object in Figure 4 can be derived as follows:

$$V_k = (r_k + j\omega L_k)I_k - j\omega(M_{am} + M_{bm})I_m \quad (3a)$$
$$V_m = -j\omega L_m I_m + j\omega(M_{am} + M_{bm})I_k = r_m I_m \quad (3b)$$

From (3), the equivalent impedance of the channel when a metal object is present can be derived as

$$Z_{eq,me} = \frac{V_k}{I_k} = r_k + j\omega L_k + \frac{\omega^2(M_{am} + M_{bm})^2}{r_m + j\omega L_m} \quad (4)$$

where the subscript "*me*" denotes "metal object." From (4), $Z_{eq,me}$ can be rewritten as

$$Z_{eq,me} = \beta r_k + j\omega\alpha L_k \quad (5)$$

where α and β are respectively the inductance variation ratio and the resistance variation ratio, as follows:

$$\alpha = 1 - \frac{L_m}{L_k} \times \frac{\omega^2(M_{am} + M_{bm})^2}{r_m^2 + \omega^2 L_m^2} \quad (6a)$$
$$\beta = 1 + \frac{r_m}{r_k} \times \frac{\omega^2(M_{am} + M_{bm})^2}{r_m^2 + \omega^2 L_m^2} \quad (6b)$$

The impedance change from (1) to (5), ΔZ_{eq}, is defined as follows:

$$\Delta Z_{eq} = \left| |Z_{eq,wo}| - |Z_{eq,me}| \right| \quad (7)$$

From (1), (5), and (7), the impedance change level, γ, of one channel can be defined as

$$\gamma = \frac{\Delta Z_{eq}}{|Z_{eq,wo}|} = \left| 1 - \sqrt{\frac{\beta^2 + \alpha^2 Q_k^2}{1 + Q_k^2}} \right| \quad (8)$$

where Q_k is the quality factor of the channel *k* and is defined as

$$Q_k = \frac{\omega L_k}{r_k} \quad (9)$$

In most cases, since the metal object has high electrical conductivity, the resistance r_m is small. Even if the metal object is as large as the Tx pad itself, r_m is still small compared to r_k. On the other hand, the resistance r_k of a sensing coil can be much higher compared to r_m due to high number of turns and small sensing wire width. Therefore, in general, r_m is much smaller than r_k, making β close to unity and γ in (8) can be rewritten as:

$$\gamma \approx \left|1-\sqrt{\frac{1/Q_k^2+\alpha^2}{1/Q_k^2+1}}\right| = 1-\sqrt{1-\frac{1-\alpha^2}{1/Q_k^2+1}} \qquad (10a)$$

However, in rare case that the metal object has high r_m comparable to r_k, the impedance change γ given in (8) should be rewritten as below:

$$\gamma = \left|1-\sqrt{\frac{\beta^2+\alpha^2 Q_k^2}{1+Q_k^2}}\right| = \left|1-\sqrt{\alpha^2+\frac{\beta^2-\alpha^2}{1+Q_k^2}}\right| \qquad (10b)$$

It can be seen from (10b) that, as r_m increases, β increases, which leads to the reduction of γ or the reduction of sensitivity. However, the effect of high r_m can be nullified by high sensing coil quality factor Q_k. If Q_k is made high enough, the impedance changes in both (10a) and (10b) can be approximated respectively as (11a) and (11b):

$$\gamma \approx \left|1-\sqrt{\frac{1/Q_k^2+\alpha^2}{1/Q_k^2+1}}\right| \approx 1-\alpha \quad \because Q_k \gg 1 \qquad (11a)$$

$$\gamma = \left|1-\sqrt{\alpha^2+\frac{\beta^2-\alpha^2}{1+Q_k^2}}\right| \approx 1-\alpha \quad \because \frac{\beta^2-\alpha^2}{1+Q_k^2} \approx 0 \qquad (11b)$$

In practice, even with a high Q_k, γ can be as low as only a few percent, making it difficult to differentiate it from noise. Accordingly, a parallel resonant circuit with an inverting amplifier is used, as shown in Figure 6, in order to enhance the detection sensitivity. In Figure 6, the sinusoidal input voltage, v_{IN}, has a frequency ω_{in} of around 1 MHz. The selection of ω_{in} is the qualitative trade-off between high sensitivity and low-noise sensing. In order to achieve high sensitivity of the sensing coil, Q_k should be high, and hence, ω_{in} should be high. However, as ω_{in} increase, the skin depth of sensing coil reduces, which increases the internal resistance of the coils. In addition, as the sensing pattern is mounted on the Tx pad, the coupling noise from the Tx coil can appear on the sensing circuit. This noise stems from the odd harmonics of the switching frequency of the IPT system, which is set as 85 *k*Hz in this paper, as recommended in [34].

To reduce the effect of these harmonics, the frequency ω_{in} should be selected higher than 85 kHz, and in between two consecutive odd harmonics of 85 kHz. The frequency ω_{in}, therefore, is selected as 1 MHz, which is high enough for high quality factor, and it is also in between 11th and 13rd order harmonics of 85 kHz for noise reduction. The switches S_1, S_2 … S_n are turned on consecutively such that only one channel is activated at one time. The series capacitors C_1, C_2, …, C_n with a sufficiently large capacitance is connected in series with the switch to block the dc component on the output voltage [33].

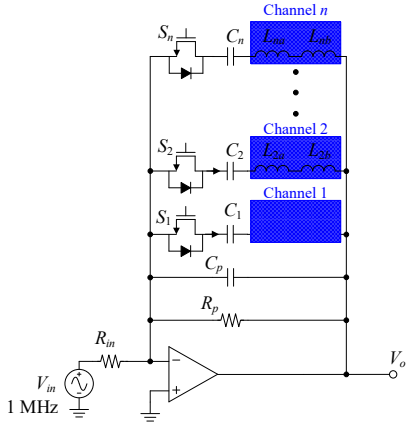

FIGURE 6. Parallel resonant circuit with an inverting op-amp amplifier to amplify the impedance change of the sensing coils due to the existence of a metal object.

When there is no metal object, the capacitor C_p resonates with L_k at ω_{in}. Thus, given that the impact of the blocking capacitor C_k and internal resistance r_k are negligible, the gain of the circuit, G, can be derived as

$$G = \frac{V_{o,wo}}{V_{in}} \approx -\frac{R_p}{R_{in}} \qquad (12)$$

where $V_{o,wo}$ is the output voltage of the op-amp when a metal object is not present. When a metal object is present, due to the change of L_k, the gain is decreased, as follow:

$$G = \frac{V_{o,me}}{V_{in}} \approx -\frac{R_p}{R_{in}} \times \frac{1}{\sqrt{1+\omega_{in}^2 C_p^2 R_p^2 \frac{(1-\alpha)^2}{\alpha^2}}} \qquad (13)$$

The detection sensitivity, S_{de}, can be defined as follow:

$$S_{de} = \left|\frac{V_{o,wo}-V_{o,me}}{V_{o,wo}}\right| \qquad (14)$$

From (12), (13), and (14), S_{de} can be derived as follow:

This article has been accepted for publication in a future issue of this journal, but has not been fully edited. Content may change prior to final publication. Citation information: DOI 10.1109/ACCESS.2020.2995210, IEEE Access

$$S_{de} = \left| 1 - \frac{1}{\sqrt{1+\omega_{in}^2 C_p^2 R_p^2 (1-\alpha)^2 / \alpha^2}} \right| \quad (15)$$

From (11) and (15), S_{de} can be defined as follow:

$$S_{de} = 1 - \frac{1}{\sqrt{1+\omega_{in}^2 C_p^2 R_p^2 \frac{\gamma^2}{(1-\gamma)^2}}} \quad (16)$$

As (16) indicates, with a proper selection of the resistor R_p, S_{de} can be much higher than γ as an example shown in Figure 7. In this example, ω_{in} = 1 MHz, C_p = 844 pF, L_k = 30 μH and R_p = 47 $k\Omega$, R_{in} = 2.4 $k\Omega$. At a high Q_k, the calculation and simulation results are nearly identical and S_{de} is much higher than γ in the small γ region (the shadowed area). However, as Q_k decreases due to an increase in r_k, S_{de} becomes increasingly lower as the slope becomes progressively more gradual. Therefore, the amplifying function of the parallel resonant circuit is valid only when Q_k is high. This proves that a high Q_k is an important design parameter not only for a high impedance-change level but also for high detection sensitivity.

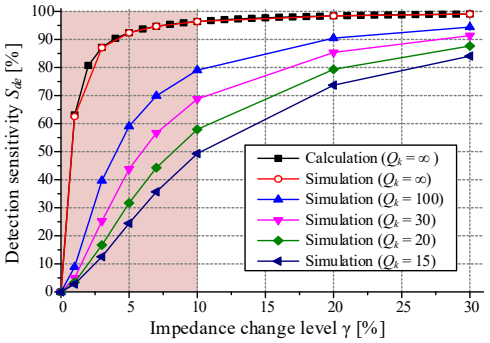

FIGURE 7. The enhancement of detection sensitivity S_{de} compared to γ owing to the resonant amplifier circuit with various quality factors Q_k of the sensing coil.

As (17) indicates, S_{de} of a channel varies with the location of the metal object. Therefore, for convenience, the detection sensitivity when a metal object is positioned at the center of a sensing coil as shown in Figure 4 is defined as the detection sensitivity of that sensing coil. In the SIRC-type conventional design [33], the S_{de} values of sensing coil a and sensing coil b of channel k are not identical. As shown in Figure 4 (a), when the metal object is positioned at the center of coil ka, there is no magnetic coupling between the metal object and coil b; hence, M_{bm} in (6a) becomes zero. The ratio α becomes α_a, as follow:

$$\alpha = \alpha_a = 1 - \frac{\omega^2 M_{am}^2}{r_m^2 + \omega^2 L_m^2} \quad (17)$$

From (11) and (17), the impedance change level becomes γ_a, as in

$$\gamma = \gamma_a \approx 1 - \alpha_a = \frac{\omega^2 M_{am}^2}{r_m^2 + \omega^2 L_m^2} \quad (18)$$

Similarly, when the metal object is on coil kb, as shown in Figure 4(b), M_{am} in (6b) becomes zero. Thus, the impedance change level becomes γ_b, as in

$$\gamma = \gamma_b \approx 1 - \alpha_b = \frac{\omega^2 M_{bm}^2}{r_m^2 + \omega^2 L_m^2} \quad (19)$$

Equations (18) and (19) show that if M_{am} and M_{bm} are different, the impedance change level and hence the detection sensitivity of sensing coil a and sensing coil b will also differ. In the conventional design, due to different number of turns, M_{am} and M_{bm} become different. Accordingly, the detection sensitivity levels of two sensing coils in channel k are not symmetric. This asymmetry is a major problem because the sensitivity of one sensing coil can be too low to overcome the noise from the IPT system.

On the other hand, in the case of the symmetric coil design, because the numbers of turns of every sensing coil in every channel are identical, M_{am} and M_{bm} are identical. Therefore, the symmetry of S_{de} in one channel is guaranteed. Furthermore, the inductances L_k of each channel are also similar, which results in similar sensitivity in every channel.

B. EQUIVALENT CIRCUIT WHEN METAL OBJECT IS ON BOTH SENSING COILS

In previous section, we have discussed the case when a metal object is on only one of the two sensing coils of one channel. This is the most often happen case during MOD operation. However, we cannot ignore the case when a metal object is on both two sensing coils of one channel as shown in Figure 8.

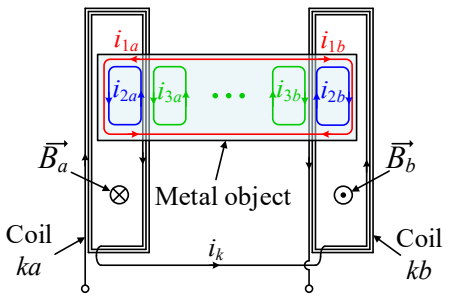

FIGURE 8. The case when the metal object is on both sensing coils of channel k.

When the metal object is on both sensing coils ka and kb of the channel k, many eddy currents i_1, i_2, i_3, and so on are generated inside the metal object by the magnetic flux of coils ka and kb as shown in Figure 8. Regarding the eddy

This article has been accepted for publication in a future issue of this journal, but has not been fully edited. Content may change prior to final publication. Citation information: DOI 10.1109/ACCESS.2020.2995210, IEEE Access

current i_1, the eddy currents i_{1a} and i_{1b} are caused by the magnetic flux of coils *ka* and *kb*, respectively. Due to opposite direction of magnetic flux density B_a and B_b, i_{1a} and i_{1b} are also of opposite direction. Therefore, if the metal object is placed exactly at the center of the two sensing coils, the magnetic flux generated by i_{1a} and i_{1b} will be cancelled out; hence, there is no impedance change on channel *k* caused by i_1. In another word, if a metal object is placed at the center of two sensing coils of one channel, there is no eddy current effect caused by i_1. The equivalent circuit of the channel with respect to i_1 can be illustrated as in Figure 9(a). As indicated in Figure 9(a), as i_{1a} is equal to i_{1b}, the total current i_1 becomes zero. Therefore, it is as if that there is no eddy current i_1.

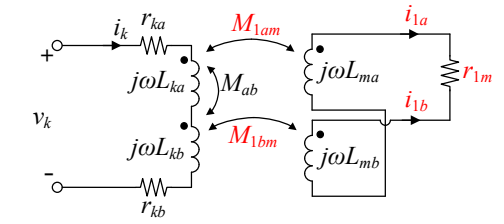

(a) with respect to eddy current i_1

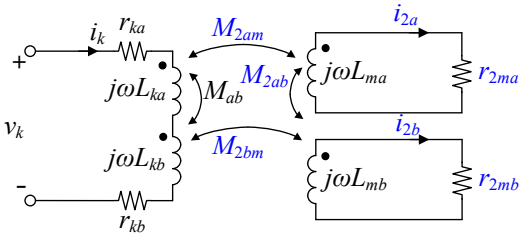

(b) with respect to eddy current i_2

FIGURE 9. The equivalent circuit of channel k with respect to each eddy current.

However, as shown in Figure 8, there is another eddy current, i_2, flowing inside the metal object. The eddy current i_{2a} caused by coil *ka* is independent from the eddy current i_{2b} caused by coil *kb*. Accordingly, they can be treated as two separated loops represented by two separated inductor-resistor series as shown in Figure 9(b). The mutual inductance between them, M_{2ab}, represents the magnetic coupling between two eddy current loops i_{2a} and i_{2b}. The effect caused by these two eddy currents can cause impedance change on the channel *k*, thus, enabling MOD system detect the metal object. Furthermore, there are another eddy currents i_3, i_4, and so on, but these currents are small in value because they are far from sensing coils. Therefore, they are negligible.

As shown in Figure 9(b), the equivalent circuit of the channel *k* with respect to i_2 can be considered as an equivalent circuit with two separated metal objects, which carry the currents i_{2a} and i_{2b}. In order to verify this analysis, an FEM simulation model is built as shown in Figure 10 with two cases. The first case is when only one single metal object is placed at the center of the two sensing coils. The second case is the two-separated-metal-object model where two metal objects are put at the center of each sensing coil. The distance, *d*, between two sensing coils are varied in order to check whether the impedance change level are different at each case. The simulation results of the impedance change level in both cases are shown in Figure 11.

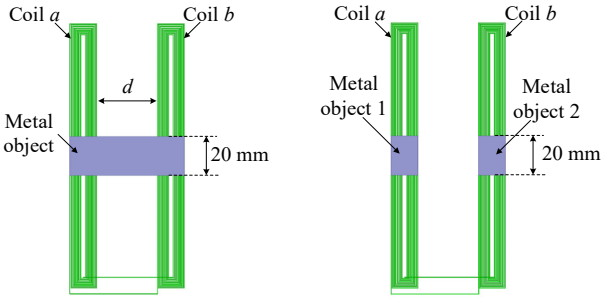

(a) case 1: when one metal object covers both sensing coils

(b) case 2: when two metal objects cover each sensing coil

FIGURE 10. Two cases of when the metal object is on both two sensing coils of channel *k*.

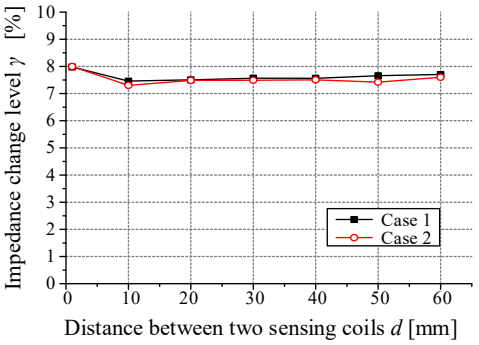

FIGURE 11. FEM simulation results in two cases of Figure 10.

From the simulation results shown in Figure 11, we can derive two following important comments:

1) Even though the metal object is placed at the center of the channel, the impedance change level is quite high, at around 7.5%, which means the metal object can be completely detected. Therefore, this is not a blind-zone, as opposed to the symmetric sensing coil in IVS type. In the IVS type, if a metal object is placed at the exact center of the channel, it cannot be detected due to same induced voltage caused by the eddy currents in both sensing coils. Therefore, a modification at the center channels of IVS is needed [32]. This is a big difference between the symmetric sensing coil of SIRC type compared to its counterpart of IVS type.
2) The implication that two separated metal object model is equivalent to one single metal object model, which is implied by the analysis, is verified by the fact that the impedance change level of both case are almost identical. Therefore, it can be said that the eddy current i_2 is the

main contribution to the impedance change of the channel.

In this analysis by the equivalent circuit considering two cases of metal object position, it is verified that the symmetric-sensitivity can be achieved with the symmetric sensing coil of the SIRC type, and that the center of a channel is not a blind-zone.

C. INFLUENCE OF MUTUAL INDUCTANCE BETWEEN SENSING COILS AND METAL OBJECT SIZE ON SENSITIVITY

As shown in Figure 5, there is a mutual coupling between coil *ka* and *kb* of channel *k*, represented by the mutual inductance M_{ab}. However, as the distance between two sensing coils increases, M_{ab} reduces significantly as shown in the FEM simulation result of the coupling coefficient between two sensing coils of the channels from channel 1 to channel 5 in Figure 12.

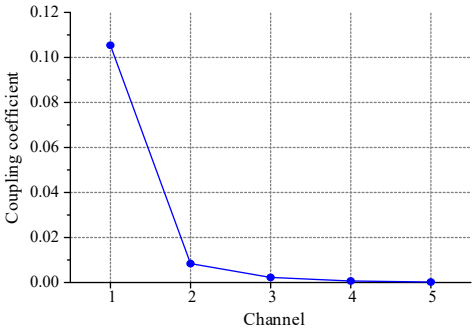

FIGURE 12. Simulation result of the coupling coefficient between two sensing coils of channels from channel 1 to channel 5.

As indicated in Figure 12, except channel 1, from channel 2 to higher numbered channel, the coupling coefficient is close to zero due to large distance between two sensing coils of one channel. Therefore, the mutual inductance M_{ab} between two sensing coils can be negligible, except in channel 1. Without M_{ab}, L_k in (2b) reduces to L_{kn}, which is defined as

$$L_{kn} = L_{ka} + L_{kb} \tag{20}$$

Accordingly, the impedance of the sensing coil without metal object, $Z_{eq,wo}$ in (1) should be rewritten as follow:

$$Z_{eq,wo} = r_k + j\omega L_{kn} \tag{21}$$

The equivalent impedance of the sensing coil with the presence of the metal object, $Z_{eq,me}$, can be obtained as in

$$Z_{eq,me} = \beta' r_k + j\omega\alpha' L_{kn} \tag{22}$$

where α' and β' are given as follows:

$$\alpha' = 1 - \frac{L_m}{L_{kn}} \times \frac{\omega^2 (M_{am} + M_{bm})^2}{r_m^2 + \omega^2 L_m^2} \tag{23a}$$

$$\beta' = 1 + \frac{r_m}{r_k} \times \frac{\omega^2 (M_{am} + M_{bm})^2}{r_m^2 + \omega^2 L_m^2} \tag{23b}$$

The impedance change level in (11), therefore, can be approximated as in

$$\gamma \approx 1 - \alpha' = \frac{L_m}{L_{kn}} \times \frac{\omega^2 (M_{am} + M_{bm})^2}{r_m^2 + \omega^2 L_m^2} \quad \because Q_k \gg 1 \tag{24}$$

It can be seen from (11) and (24) that without the mutual inductance M_{ab}, the impedance change level seems to increase due to reduced L_k. However, when the M_{ab} increases, which means the two sensing coils are close to each other as in case of channel 1, the M_{am} and M_{bm} can be both non-zero since a metal object can affect both sensing coils. This can increase the impedance change level as dictated in (24). On the other hand, in case M_{ab} is negligible, the two sensing coils are far from each other; hence, the impedance change level will become either (18) or (19). Therefore, the impedance change level of the channel 1 may become bigger than the other channel.

Regarding the mutual inductance between two adjacent channel, as indicated in Figure 6, by controlling the switches S_1, S_2, …, S_n, only one channel is activated at one time. Therefore, during the time one channel is activated, all the other channels are disconnected from the sensing circuit by the switches. Accordingly, since there is no current flowing through any channel except the activated channel, the mutual coupling effect between channels is eliminated. In other words, the sensing coils are operated by a time-division controller so that only one channel is activated at one time. Thus, the effect of the mutual coupling between adjacent channels exists is eliminated. Moreover, such design of the sensing circuit also minimize the influence of the sensing coils on the efficiency of the IPT system. The power loss inflicted by the sensing coil is attributed to only one activated channel because all the other deactivated channels are open circuit. Therefore, the power loss caused by the sensing coil becomes small.

According to (11), the impedance change level γ of the proposed sensing coil is proportional to the mutual inductances M_{am} and M_{bm}. These mutual inductances, in turns, are proportional to the area of the sensing coil covered by the metal object. Therefore, in general, as the size of the metal object increases, the area of sensing coil covered by the metal object increases, which ultimately leads to the increase of γ due to the increase of M_{am} and M_{bm}. However, the increase of γ due to the increase of metal object size is directional. Figure 13(a) shows a metal object with the length l_m and the width

w_m covers a sensing coil. An FEM simulation is conducted with different l_m and w_m as shown in Figure 13(b). The simulation results show that the increase rate of γ with respect to l_m is higher than that with respect to w_m. In detail, when l_m is kept constant at 20 mm, as w_m exceeds the width of the coil w_{coil} at 13.5 mm, γ increases very slowly. This is because the area covered by the metal object does not change when w_m exceeds 13.5 mm. In contrast, when w_m is kept constant at 20 mm, as long as l_m is smaller than the length of the coil l_{coil}, the area cover by metal object increases proportionally to the increase of l_m, leading to the increase of γ.

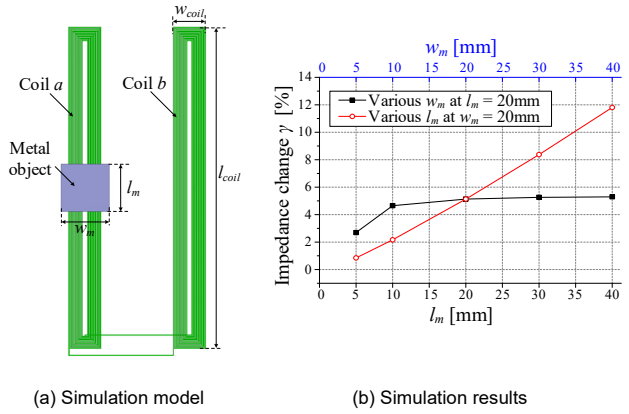

(a) Simulation model (b) Simulation results

FIGURE 13. FEM simulation with w_{coil} = 13.5 mm, l_{coil} = 150 mm, and number of turns is 12, to verify the influence of metal object size on sensitivity.

IV. DESIGN OF THE PROPOSED SYMMETRIC SENSING COILS

In the paper, the target minimum size of a metal object is 20mm × 20mm. Thus, the sensing coil should be designed so that it can detect such a metal object everywhere on the surface of the Tx pad. Therefore, to guarantee that S_{de} is high enough to overcome the high-frequency noise from the IPT system with such a small metal object, the impedance change level of a sensing coil should exceed a predefined threshold of 2.5% while the number of channels should be minimized to reduce the complexity of the sensing circuit. These are two criteria of this optimization problem.

Figure 14 shows two channels k and m, which are placed next to each other. When the metal object is placed at the center of sensing coils (point A_1 or A_2), γ becomes highest due to the highest value of M_{am} or M_{bm}. When the metal object is positioned between two channels (point B), γ becomes lowest. The target of the design is to set the impedance change level at point A, called γ_A, higher than 5%, and the impedance change level at point B, called γ_B, higher than the threshold of 2.5%. These thresholds are defined based on knowledge of the amplitude of noise in an IPT system for WEV charging.

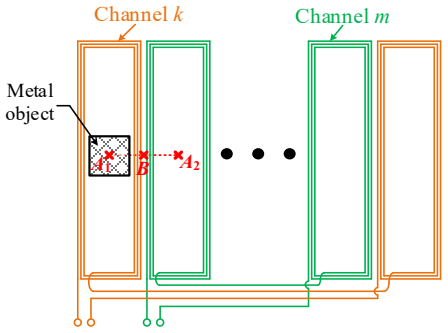

FIGURE 14. Change in the detection sensitivity *S* depending on the position of a metal object. When the metal object is at the center of the sensing coils (A_1 or A_2), *S* becomes highest. When the metal object is between two adjacent sensing coils (point *B*), *S* becomes lowest.

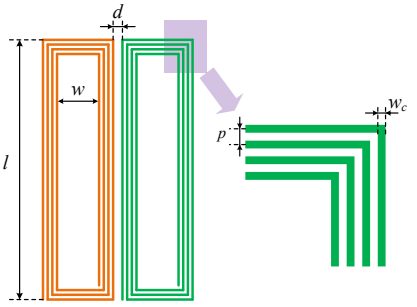

FIGURE 15. Dimensions of sensing coils that must be optimized for maximum detection sensitivity at every position of a metal object.

All of the dimensions of sensing coils that needed to be designed are shown in Figure 15. In the figure, the distance between two adjacent sensing coils, d, is determined to be 1 mm in order to maximize γ_B. The width of the sensing wire, w_c, is determined to be 0.25 mm considering the trade-off between the low coil resistance r_k and the low eddy current caused by the magnetic field from the Tx coil. The pitch p should be wide enough to mitigate the proximity effect between the turns but also narrow enough to enhance the coupling between the metal object and the sensing coil. Thus, p is set to 0.5 mm. The remaining dimensions are the length of the sensing coil l, the inner width of the sensing coil w, and the number of turns N.

Increasing l and w will reduce the coupling coefficient between the metal object and the sensing coils, but this can also reduce the number of channels. On the other hand, increasing N may increase γ_A, whereas this can reduce γ_B. Therefore, to design the sensing coils is to optimize N, w, and l considering the balance between a high impedance change level when the metal object is at any location and with a low number of channels. To optimize the design of the sensing coil based on variations of N, w, and l, an FEM simulation model of a sensing coil and a 20 mm × 20 mm metal object were built in ANSYS Maxwell 15.2, as shown in Figure 16. The impedance change level of the sensing coil is tested at the two metal object locations: at the center of the coil, as shown in Figure 16(a), and between two adjacent coils, as

This article has been accepted for publication in a future issue of this journal, but has not been fully edited. Content may change prior to final publication. Citation information: DOI 10.1109/ACCESS.2020.2995210, IEEE Access

shown in Figure 16(b).

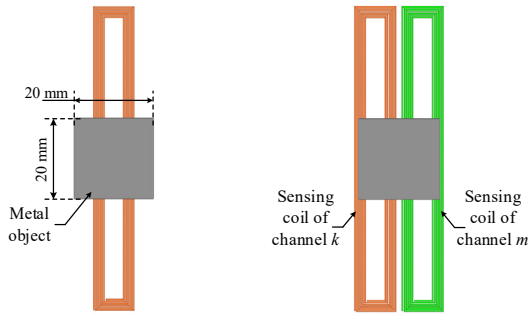

(a) Metal object is at the center of the coil

(b) Metal object is between two adjacent coils

FIGURE 16. FEM simulation model of a sensing coil and metal object in ANSYS Maxwell 15.2. The number of turns of the sensing coil *N*, the length of the sensing coil *l*, and the inner width of the sensing coil *w* will be varied to determine to the optimal design based on the criterion of the highest value of *γ* at two locations of the metal object.

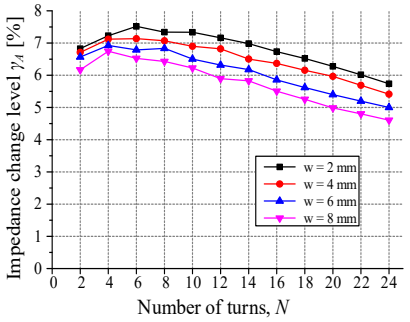

(a) l = 100 mm

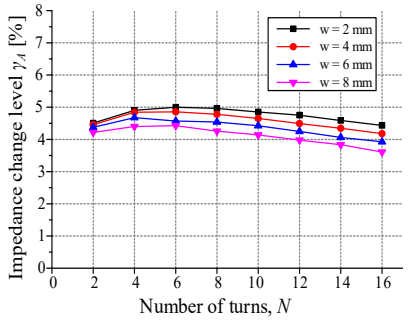

(b) l = 150 mm

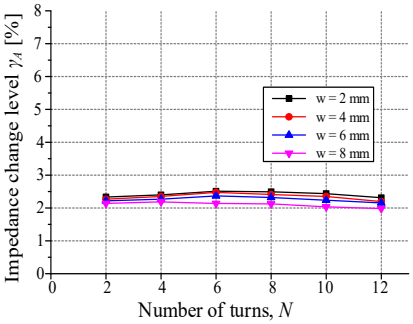

(c) l = 300 mm

FIGURE 17. Impedance change level γ_A with various values *w* and *N* with the metal object at the center position of the coil.

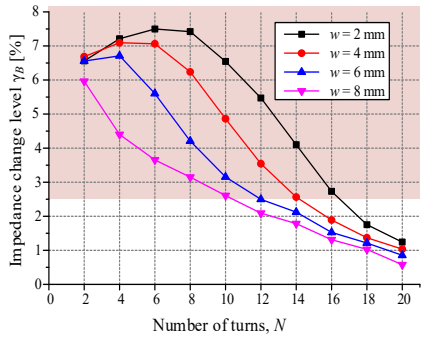

(a) l = 100 mm

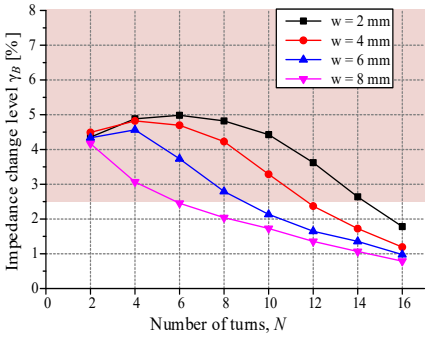

(b) l = 150 mm

FIGURE 18. Impedance change level γ_B with various values of *w* and *N* with the metal object between two adjacent sensing coils.

The simulation results are shown in Figures 17 and 18. In Figure 17, the metal object is positioned at the center of the sensing coil. It is shown that with each length of the sensing coil from 100 mm to 300 mm, there are optimal points at which the sensitivity is maximized. In Figure 17(c), when l is 300 mm, the maximum γ_A is lower than 2.5%, much lower than the target of 5%, invalidating it as a solution for the design. When l equals 100 mm and 150 mm, as indicated correspondingly in Figures 17(a) and (b), when N and w increases, γ_A decreases. When l = 100 mm, the sensitivity is well above 5% until N reaches 24 turns. However, when l = 150 mm, N should be limited between four and twelve turns, while w should be limited between 2 mm and 4 mm in order to guarantee that γ_A equals 5%.

Figure 18 shows the simulation results of the impedance change level γ_B when the metal object is between two adjacent sensing coils. Similar to the simulation results shown in Figure 3.20, when the number of turns and the inner width increase, γ_B decreases. Therefore, N and w should be limited to guarantee that γ_B has a minimum rate of 2.5%. On the other hand, N and w should be as large as possible to minimize the number of channels.

In order to consider the number of channels, n, as one of the criteria to optimize the coil design, a figure of merit (FoM) equation has been built as below:

$$FOM = \frac{\gamma_A + \gamma_B}{n} \tag{25}$$

where n is the number of channel, which is inversely proportional to the FoM, while γ_A and γ_B are given the same weighing coefficient and proportional to the FoM. The results of FoM in cases of l = 100 mm and l = 150 mm are shown in Figures 19(a) and 19(b), respectively.

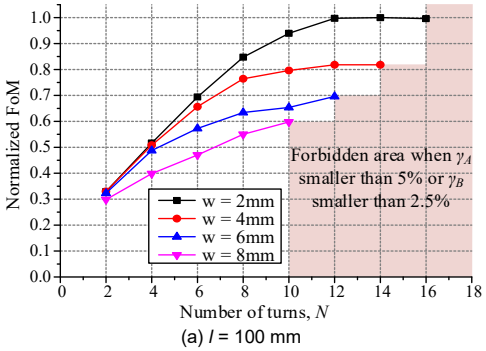

(a) *l* = 100 mm

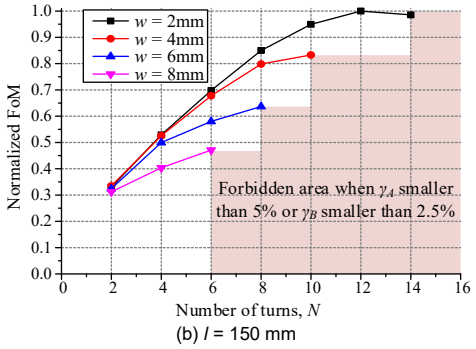

(b) *l* = 150 mm

FIGURE 19. Normalized figure of merit (FoM) plot for two cases.

As indicated in Figure 19(a), when l = 100 mm, the FoM is highest at N = 14 turns and w = 4 mm. With l = 150 mm, according to Figure 19(b), N = 12 turns and w = 2 mm is where the FoM reaches the highest value. Therefore, the optimized design coil can be either l = 100 mm, N = 14 turns, and w = 2 mm, or l = 150 mm, N = 12 turns, and w = 2 mm, corresponding to 112 and 96 channels, respectively. In this dissertation, the latter design is selected.

V. EXPERIMENTAL VERIFICATION

In order to verify the performance of the proposed symmetric sensing coil design, an IPT system for WEV charging together with an MOD system were built. The IPT system is shown in Figure 20.

In this research, the Tx pad is designed loosely based on the R-GA-2 specification, and the Rx pad is designed loosely based on R-VA-WPT2/Z3 specification recommended in the standard SAE J2954 proposed in May, 2016 [34]. To prove the feasibility of the proposed MOD system, the power level used to test the FOD system is 3.3 kW, which is compatible with WPT1 power class with the Tx current of 20 A_{rms}. However, based on the analysis, the proposed MOD system theoretically can work with any power level, even with WPT3 class, when the power is 10 kW and the Tx current is 50 A. However, the problem with higher power is that the coupling noise from the Tx coil to the sensing pattern can degrade the performance of the MOD system. This problem can be solved by a proper design of an electrostatic shield between Tx pad and sensing pattern. To minimize the loss caused by eddy current in the shield, the electrostatic shield can be designed as many comb-pattern copper metal strips instead of a large metal sheet. The design of the electrostatic shield, however, is out of scope of this paper.

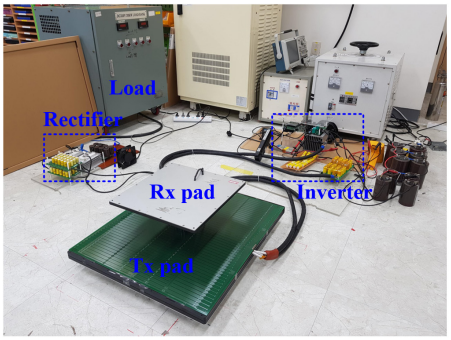

FIGURE 20. Prototype of the inductive power transfer system for stationary WEV charging.

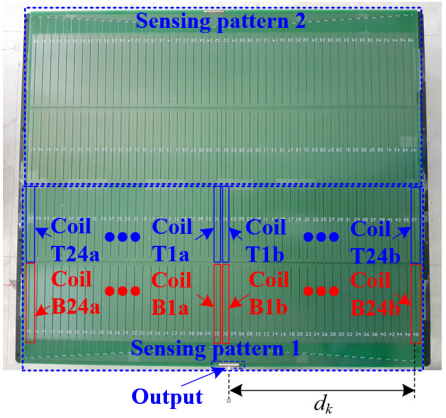

(a) Proposed symmetric sensing patterns. Each sensing pattern includes 48 channels and two rows, covering half of the Tx pad.

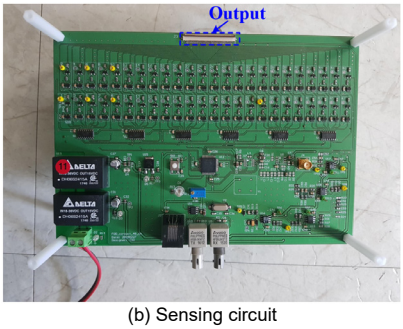

(b) Sensing circuit

FIGURE 21. Metal object detection system with the proposed symmetric sensing coil and sensing circuit.

On the other hand, the MOD system is composed of the proposed sensing coils and a sensing circuit, as shown in Figure 21. To fit the size of the Tx pad, two identical sensing patterns are designed; each of them includes 48 channels and covers half of the Tx pad, as shown in Figure 21(a). As indicated in Figure 21(a), the sensing pattern 1 includes 48 channels, which are divided into two rows. The bottom row includes channels from B1 to B24 where the letter "B" stands for "bottom"; the top row includes channels from T1 to T24, where letter "T" stands for "top". All the channels are connected to the sensing circuit through the outputs as shown in Figures 21(a) and (b). The parameters of both the IPT system and the MOD system are shown in Table I.

TABLE I
PARAMETERS OF THE IPT AND MOD SYSTEMS

Parameter	Value
Tx pad size	700mm × 600mm
Rx pad size	400mm × 400mm
Air gap between Tx and Rx pads	150 mm
Switching frequency of IPT system	85 *k*Hz
Tx current (RMS)	20 A
Sensing coil size (l, w, N)	150 mm, 2 mm, 12 turns
Number of channels	48 × 2
Size of metal object (aluminum)	20 mm × 20 mm × 1 mm
Power level	3.3 kW
DC-DC efficiency without sensing pattern	87.8 %
DC-DC efficiency with sensing pattern	86.9 %

A. SYMMETRIC SENSITIVITY VERIFICATION

Due to the symmetry of the Tx pad and because the two sensing patterns are identical, it is sufficient to assess the near-uniform sensitivity in the sensing pattern 1.

Figures 22(a) and (b) show the measurement results of channel self-inductances and quality factors of sensing pattern 1. As explained in section III.C and Figure 12, due to high mutual inductance between two sensing coils of channel 1, the equivalent inductance of channel 1 is higher than that of channel 2, where the mutual inductance is close to zero, as shown in Figure 22. It is shown that as the channel position moves farther from the output, the inductance does not change much due to identical number of turns in each channel. The slightly gradual increase of the channel inductance is probably caused by the increased distance between the sensing coils to the output as shown in Figure 21(a). As indicated in the figure, as the channel goes further to the edge of the Tx pad, the distance d_k between the sensing coils to the output increases. The sensing coils of channel 24, therefore, is much farther from the output than those of channel 2. Considering the size of the Tx pad, this can contribute to a slight difference in inductance among channels. This increase of d_k also increases the equivalent series resistance (ESR) of channel, which reduces the quality factor of channel as channel position moves towards the edge of Tx pad. As the result, the detection sensitivity of channels also reduces as the channel position moves farther from the output as the experimental results shown in Figure 23. In this experiment, a metal object 20 mm × 20 mm in size is placed at the center of coil *a* and coil *b* of every channel from T1 to T24, as well as from B1 to B24. The corresponding detection sensitivity of the coil at each position is measured and shown in Figure 23. For example, when the metal object is placed at coil *a* of bottom channel B8, the corresponding detection sensitivity can be found at bottom row sensing coil 8*a* in Figure 23.

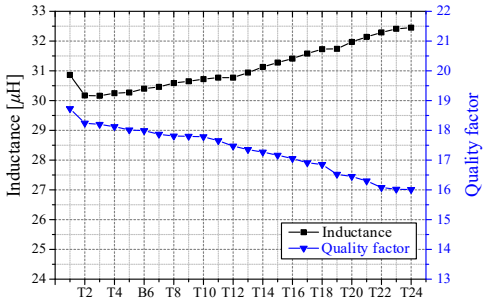

(a) Channels on top row: from T1 to T24

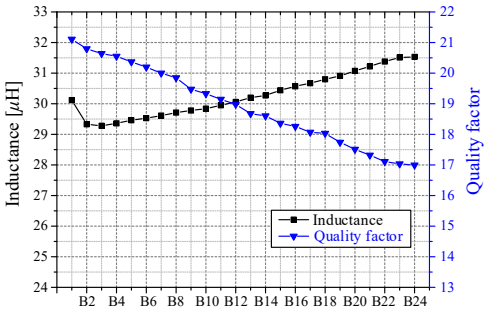

(b) Channels at bottom row: from B1 to B24

FIGURE 22. The inductances and quality factors of every channel in sensing pattern 1.

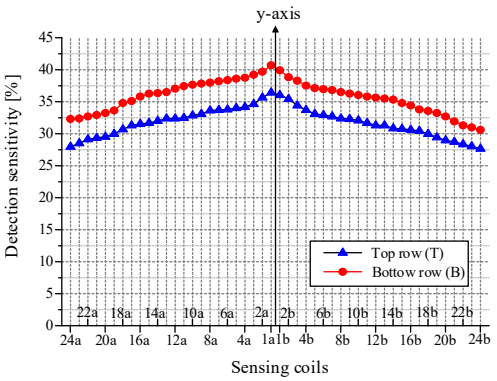

FIGURE 23. Symmetric detection sensitivity of two sensing coils *a* and *b* of each channel: top row channels from T1 to T24 (triangle symbol), and bottom row channels from B1 to B24 (circle symbol).

As shown in Figure 23, the detection sensitivity of two sensing coils of one channel is symmetric. For instance, the detection sensitivity of sensing coils 8*a* and 8*b* of bottom channel B8 are respectively 38.0% and 36.5%, which are only 1.5% different from each other. Moreover, another big advantage is that the sensitivity of all channels are close to each other. At the top row, the sensitivity fluctuates between 27.5% and 36%, while at the bottom row, the sensitivity fluctuates between 30% and 42%. This symmetry is the result of same number of turns in every channel, which makes the quality factor fluctuation in all channel is small as shown in Figure 22. This proves the proper performance of the proposed symmetrical sensing coil design.

B. BLIND-ZONE-FREE VERIFICATION

To test the blind-zone-free feature of the proposed sensing coils design, an experiment was conducted with a 20 A Tx current to test the sensitivity over the entire surface of the Tx pad. In this experiment, a metal object 20 mm × 20 mm in size is placed at many measurement points. The map of these measurement points is shown in Figure 24(a).

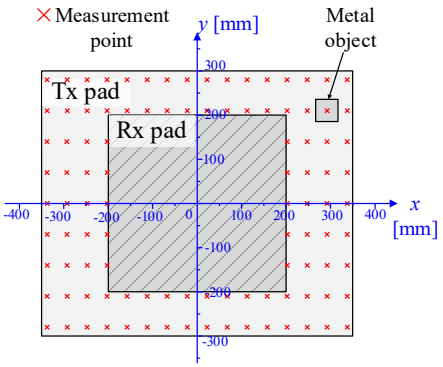

(a) Metal object position diagram

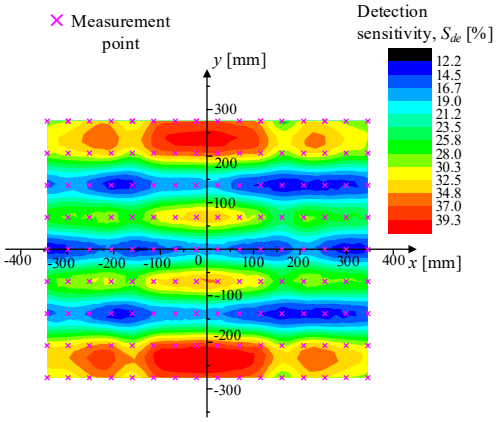

(b) Spectrum of the detection sensitivity corresponding to the position of the metal object

FIGURE 24. Experimental results of the detection sensitivity with different positions of the metal object on the Tx pad at 20 A Tx current.

When the metal object is placed at one point, the detection sensitivity corresponding to that point is measured. After placing the metal object at every point in Figure 24(a), the values of the detection sensitivity at every point are presented as shown in Figure 24(b). It is noted that Figure 24 does not show the way to identify the location of the metal object because the paper only focuses on detecting the presence of metal object, which is the prime purpose of any MOD system. The location of metal object, therefore, is out of scope of the paper. As shown in Figure 24(b), the distribution of S_{de} is symmetric about the y-axis, as predicted by the analysis. Moreover, when the metal object is positioned between two rows of channels in one sensing pattern or between two sensing patterns, the detection sensitivity becomes low because at these positions, the coupling between the metal object and the sensing coil becomes lowest. Except these areas, which cover small area of the Tx pad, the sensitivity of the rest area only fluctuates between 26% and 40%. This small fluctuation cannot be achieved by the conventional sensing coil design. Even with these low detection sensitivity area, the S_{de} is 12.2% at minimum and 39.3% at maximum, which are high enough that the metal object can be detected everywhere on the Tx pad, proving the blind-zone elimination feature of the proposed sensing coils.

As indicated in Figure 24(b), it is noted that when the metal object is placed at the center of the two sensing coils of channel T1 or channel B1, the detection sensitivity becomes higher because both mutual inductances M_{am} and M_{bm} are different from zero. Therefore, both M_{am} and M_{bm} contribute to the impedance change as equations (11a) and (11b) indicate.

VI. CONCLUSION

The concept and design of the proposed symmetric sensing coil, which is adapted to SIRC-based MOD system, was introduced and analyzed. Through the proposed equivalent circuit based analysis, it was found that the symmetric sensing coil design for SIRC method is different from that for IVS type. Moreover, the analysis clarifies the influence of sensing coil quality factor, metal object size, and symmetric sensing coil concept on the detection sensitivity of the SIRC method. Based on the analysis, a design optimization for proposed sensing coils was made for highest sensitivity and lowest number of channels and validated by experiments with a 20 A_{rms} Tx current and a 20 mm × 20 mm metal object. As such, the proposed symmetric sensing coil promises to be an inexpensive and effective solution for MOD systems for WEV chargers.

REFERENCES

[1] G. A. Covic and J. T. Boys, "Modern Trends in Inductive Power Transfer for Transportation Applications," *IEEE Journal of Emerging and Selected Topics in Power Electronics*, vol. 1, no. 1, pp. 28-41, March 2013.

[2] S. Y. R. Hui, W. Zhong, and C. K. Lee, "A Critical Review of Recent Progress in Mid-Range Wireless Power Transfer," *IEEE Transactions on Power Electronics*, vol. 29, no. 9, pp. 4500-4511, Sept. 2014.

[3] S. Li and C. C. Mi, "Wireless Power Transfer for Electric Vehicle Applications," *IEEE Journal of Emerging and Selected Topics in Power Electronics*, vol. 3, no. 1, pp. 4-17, March 2015.
[4] Su Y. Choi, Beom W. Gu, Seog Y. Jeong, and Chun T. Rim, "Advances in Wireless Power Transfer Systems for Roadway-Powered Electric Vehicles," *IEEE Journal of Emerging and Selected Topics in Power Electronics*, vol. 3, no. 1, pp. 18-36, March 2015.
[5] C. C. Mi, G. Buja, S Y. Choi, and Chun T. Rim, "Modern Advances in Wireless Power Transfer Systems for Roadway Powered Electric Vehicles," *IEEE Transactions on Industrial Electronics*, vol. 63, no. 10, pp. 6533-6545, Oct. 2016.
[6] V. Cirimele, M. Diana, F. Freschi, and M. Mitolo, "Inductive Power Transfer for Automotive Applications: State-of-the-Art and Future trends," *IEEE Transactions on Industry Applications*, vol. 54, no. 5, pp. 4069-4079, Sept.-Oct. 2018.
[7] J. Huh, Sung W. Lee, Woo Y. Lee, Gyu H. Cho, and Chun T. Rim, "Narrow-width Inductive Power Transfer System for Online Electrical Vehicles," *IEEE Transactions on Power Electronics*, vol. 26, no. 12, pp. 3666-3679, Dec. 2011.
[8] M. Kim, D. Joo, and B. K. Lee, "Design and Control of Inductive Power Transfer System for Electric Vehicles Considering Wide Variation of Output Voltage and Coupling Coefficient," *IEEE Transactions on Power Electronics*, vol. 34, no. 2, pp. 1197-1208, Feb. 2019.
[9] L. Zhao, D. J. Thrimawithana, U. K. Madawala, A. P. Hu and C. C. Mi, "A Misalignment-Tolerant Series-Hybrid Wireless EV Charging System With Integrated Magnetics," *IEEE Transactions on Power Electronics*, vol. 34, no. 2, pp. 1276-1285, Feb. 2019.
[10] D. H. Tran, V. B. Vu and W. Choi, "Design of a High-Efficiency Wireless Power Transfer System With Intermediate Coils for the On-Board Chargers of Electric Vehicles," *IEEE Transactions on Power Electronics*, vol. 33, no. 1, pp. 175-187, Jan. 2018.
[11] R. Tavakoli and Z. Pantic, "Analysis, Design, and Demonstration of a 25-kW Dynamic Wireless Charging System for Roadway Electric Vehicles," *IEEE Journal of Emerging and Selected Topics in Power Electronics*, vol. 6, no. 3, pp. 1378-1393, Sept. 2018.
[12] S. Y. Choi, B. W. Gu, S. W. Lee, W. Y. Lee, J. Huh and C. T. Rim, "Generalized Active EMF Cancel Methods for Wireless Electric Vehicles," *IEEE Transactions on Power Electronics*, vol. 29, no. 11, pp. 5770-5783, Nov. 2014.
[13] H. Kim et al., "Design of magnetic shielding for reduction of magnetic near field from wireless power transfer system for electric vehicle," in *2014 International Symposium on Electromagnetic Compatibility*, Gothenburg, Sweden, 2014, pp. 53-58.
[14] M. Lu and K. D. T. Ngo, "Attenuation of Stray Magnetic Field in Inductive Power Transfer by Controlling Phases of Windings' Currents," *IEEE Transactions on Magnetics*, vol. 53, no. 9, pp. 1-8, Sept. 2017.
[15] M. Lu and K. D. T. Ngo, "A Fast Method to Optimize Efficiency and Stray Magnetic Field for Inductive-Power-Transfer Coils Using Lumped-Loops Model," *IEEE Transactions on Power Electronics*, vol. 33, no. 4, pp. 3065-3075, April 2018.
[16] S. Fukuda, H. Nakano, Y. Murayama, T. Murakami, O. Kozakai and K.Fujimaki, "A novel metal detector using the quality factor of the secondary coil for wireless power transfer systems," in *IEEE International Microwave Workshop Series on Innovative Wireless Power Transmission: Technologies, Systems, and Applications (IMWS)*, Kyoto, Japan, 2012, pp. 241-244.
[17] H. Kudo, K. Ogawa, N. Oodachi, N. Deguchi, "Detection of a metal obstacle in wireless power transfer via magnetic resonance," in *IEEE 33rd International Telecommunications Energy Conference (INTELEC)*, Amsterdam, Netherlands, 2011, pp. 1-6.
[18] Maikawa Kengo et al., "Non-contact power supply device," *Japanese Patent Appl.* 2011-118663, May 27, 2011.
[19] Z. N. Low, J. J. Casanova, P. H. Maier, J. A. Taylor, R. A. Chinga, and J. Lin, "Method of load/fault detection for loosely coupled planar wireless power transfer system with power delivery tracking," *IEEE Transactions on Industrial Electronics*, vol. 57, no. 10, pp. 1478-1486, Apr. 2010.
[20] M. Moghaddami and A. I. Sarwat, "A Sensorless Conductive Foreign Object Detection for Inductive Electric Vehicle Charging Systems Based on Resonance Frequency Deviation," in *IEEE Industry Applications Society Annual Meeting (IAS)*, Portland, OR, USA, 2018, pp. 1-6.
[21] N. Kuyvenhoven, C. Dean, J. Melton, J. Schwannecke, A. E. Umenei, "Development of a foreign object detection and analysis method for wireless power systems," in *IEEE Symposium on Product Compliance Engineering (IPSES)*, San Diego, CA, USA, 2011, pp. 1-6.
[22] Karanth Avinash *et al*, "Foreign object detection in inductive coupled wireless power transfer environment using thermal sensors," European Patent Appl. 2591535, Jul. 7, 2010.
[23] Katherine L. Hall *et al*, "Vehicle charger safety system and method," U.S. Patent Appl. 2011-0074346, March 31, 2011.
[24] X. Qunyu, N. Huansheng, C. Weishi, "Video-based foreign object debris detection," in *IEEE International Workshop on Imaging Systems and Techniques*, Shenzen, China, 2009, pp. 119 -122.
[25] G. Ombach, "Design considerations for wireless charging system for electric and plug-in hybrid vehicles," in *IEEE Hybrid and Electric Vehicles Conference (HEVC 2013)*, London, UK, 2013, pp.1-4.
[26] M. Ferri, G. Giunta, A. Banelli and D. Neri, "Millimeter wave radar applications to airport surface movement control and foreign object detection," in *Proceeding of the 6th European Radar Conference*, Rome, Italy, 2009, pp. 437 – 440.
[27] J. Jeong, S. Ryu, B. Lee and H. Kim, "Tech tree study on foreign object detection technology in wireless charging system for electric vehicles," in *IEEE International Telecommunications Energy Conference (INTELEC)*, Osaka, Japan, 2015, pp. 1-4.
[28] Simon Verghese, Morris P. Kesler, Katherine L. Hall, and Herbert Toby Lou, "Foreign object detection in wireless energy transfer systems," U.S. Patent 20130069441 A1 (Witricity Corporation), Sept. 9, 2011.
[29] S. Y. Jeong, H. G. Kwak, G. C. Jang, S. Y. Choi and C. T. Rim, "Dual-Purpose Nonoverlapping Coil Sets as Metal Object and Vehicle Position Detections for Wireless Stationary EV Chargers," *IEEE Transactions on Power Electronics*, vol. 33, no. 9, pp. 7387-7397, Sept. 2018.
[30] G. C. Jang, S. Y. Jeong, H. G. Kwak and C. T. Rim, "Metal object detection circuit with non-overlapped coils for wireless EV chargers," in *IEEE 2nd Annual Southern Power Electronics Conference (SPEC)*, Auckland, New Zealand, 2016, pp. 1-6.
[31] M. R. Sonapreetha, Seog Y. Jeong, Su Y. Choi and Chun T. Rim, "Dual-purpose non-overlapped coil sets as foreign object and vehicle location detections for wireless stationary EV chargers," in *IEEE PELS Workshop on Emerging Technologies: Wireless Power (WoW)*, 2015, Daejeon, South Korea, June 5-6, pp. 1-7.
[32] Van X. Thai, G. C. Jang, S. Y. Jeong, J. H. Park, Y.-S. Kim and Chun T. Rim, "Symmetric Sensing Coil Design for the Blind-zone Free Metal Object Detection of a Stationary Wireless Electric Vehicles Charger," *IEEE Transactions on Power Electronics*, vol. 35, no. 4, pp. 3466-3477, Apr. 2020.
[33] S. Y. Jeong, V. X. Thai, J. H. Park and C. T. Rim, "Self-Inductance-Based Metal Object Detection With Mistuned Resonant Circuits and Nullifying Induced Voltage for Wireless EV Chargers," *IEEE Transactions on Power Electronics*, vol. 34, no. 1, pp. 748-758, Jan. 2019.
[34] *Wireless Power Transfer for Light-Duty Plug-In/Electric Vehicles and Alignment Methodology*, document SAE TIR J2954_201605, 2016.

Van X. Thai (S'15-M'20) received the B.S. degree in electrical engineering from Hanoi University of Science and Technology, Hanoi, Vietnam in 2010, the M.S. degree in nuclear and quantum engineering from Korea Advanced Institute of Science and Technology (KAIST), Daejeon, South Korea, in 2013, and the Ph.D. degree in electrical engineering in Gwangju Institute of Science and Technology (GIST), Gwangju, South Korea, in 2020. He is currently a staff engineer at OceansBio, Seoul, South Korea.

His research interests include power converters, wireless power transfer and foreign object detection systems.

Jun H. Park (S'17) received the B.S. degree in electronic engineering from Hanyang University, Seoul, South Korea in 2017, and the M.S. degree from Gwangju Institute of Science and Technology (GIST), Gwangju, South Korea in 2019. He is currently working as an engineer at Samsung Electronics, Seoul, South Korea.

His current research interests include roadway-powered electric vehicles and wireless power transfer.

Seog Y. Jeong (S'14-M'18) received the B.S. degree in electrical engineering from Kyungpook National University, Daegu, South Korea, in 2012, and the M.S. and Ph.D. degree in Nuclear Quantum Engineering from Korea Advanced Institute of Science and Technology (KAIST), Daejeon, South Korea, in 2015 and 2018, respectively. He is currently a staff engineer at Samsung Electronics, Seoul, South Korea.

His current research interests include Roadway-Powered Electric Vehicle (RPEV) and wireless power transfers (WPT).

Chun T. Rim (M'90-SM'11-F'20) received the B.S. degree with Honor in EE from the Kumoh Institute of Technology (KIT), South Korea, in 1985, and the M.S. and Ph.D. degrees in EE from the Korea Advanced Institute of Science and Technology (KAIST), South Korea, in 1987 and 1990, respectively.

He was an Associate Professor with KAIST in 2007-2016, and a Full Professor with the Gwangju Institute of Science and Technology (GIST), South Korea, in 2016-2018. He is currently the President of the Korea Institute of Energy Technology Evaluation and Planning (KETEP). He has authored or coauthored 185 technical papers, written 16 books, and holds 160 patents (awarded and pending).

Dr. Rim won numerous awards, including the Best Paper Award of IEEE TPEL in 2015 and J-ESTPE in 2016 both in wireless power transfer (WPT). He is now a Co-Editor in Chief of IEEE TRANSACTIONS ON POWER ELECTRONICS (TPEL) and an Associate Editor of IEEE JOURNAL OF EMERGING AND SELECTED TOPICS IN POWER ELECTRONICS (J-ESTPE). He is also a Guest Editor of the Special Issue on WPT of the of IEEE TPEL, IEEE TRANSACTIONS ON INDUSTRIAL ELECTRONICS, and IEEE J-ESTPE, and a General Chair/Co-Chair of the IEEE Workshop on Wireless power (WoW) from 2015.

Yun-Su Kim (S'14-M'16) received the B.S. and Ph.D. degrees in electrical engineering from Seoul National University, Seoul, South Korea, in 2010 and 2016, respectively. He worked for Korea Electrotechnology Research Institute as a Senior Researcher from 2015 to 2017.

In 2018, he joined the Faculty of the Gwangju Institute of Science and Technology (GIST), Gwangju, South Korea, where he is currently an Assistant Professor with the School of Integrated Technology. He is the Director of the *Korean Society for New and Renewable Energy* (KSRNE) and the Editorial Director of the *Korean Institute of Electrical Engineers* (KIEE).

His research interests include distribution system, distributed generation, microgrid, artificial intelligence, and wireless power transfer.

.